



HAL
open science

THREE-DIMENSIONAL ARCHITECTURE OF NEPHRONS IN THE NORMAL AND CYSTIC KIDNEY

Thomas Blanc, Nicolas Goudin, Mohamad Zaidan, Meriem Garfa Traore,
Frank Bienaime, Lisa Turinsky, Serge Garbay, Clément Nguyen, Martine
Burtin, Gérard Friedlander, et al.

► **To cite this version:**

Thomas Blanc, Nicolas Goudin, Mohamad Zaidan, Meriem Garfa Traore, Frank Bienaime, et al..
THREE-DIMENSIONAL ARCHITECTURE OF NEPHRONS IN THE NORMAL AND CYSTIC
KIDNEY. *Kidney International*, 2020, 10.1016/j.kint.2020.09.032 . hal-03051483

HAL Id: hal-03051483

<https://hal.science/hal-03051483>

Submitted on 10 Mar 2023

HAL is a multi-disciplinary open access archive for the deposit and dissemination of scientific research documents, whether they are published or not. The documents may come from teaching and research institutions in France or abroad, or from public or private research centers.

L'archive ouverte pluridisciplinaire **HAL**, est destinée au dépôt et à la diffusion de documents scientifiques de niveau recherche, publiés ou non, émanant des établissements d'enseignement et de recherche français ou étrangers, des laboratoires publics ou privés.



Distributed under a Creative Commons Attribution - NonCommercial 4.0 International License

[QUERY TO AUTHOR: title and abstract rewritten by Editorial Office – not subject to change]

THREE-DIMENSIONAL ARCHITECTURE OF NEPHRONS IN THE NORMAL AND CYSTIC KIDNEY

Thomas Blanc^{1,2#}, Nicolas Goudin^{3#}, Mohamad Zaidan^{1,4#}, Meriem Garfa Traore³,
Frank Bienaime^{1,5}, Lisa Turinsky¹, Serge Garbay¹, Clément Nguyen¹, Martine Burtin¹,
Gérard Friedlander^{1,6}, Fabiola Terzi^{1*}, Marco Pontoglio^{1*}

Equally contributed as first author

* Equally contributed as last author and co-corresponding authors

- 1 Institut National de la Santé et de la Recherche Médicale U1151, Centre National de la Recherche Scientifique UMR8253, Université de Paris, Institut Necker Enfants Malades, Département « Croissance et Signalisation », Paris, France.
- 2 Service de Chirurgie Viscérale et Urologie Pédiatrique, AP-HP, Hôpital Necker Enfants Malades, Paris, France.
- 3 Structure Fédérative de Recherche Necker, US24-UMS3633, Paris, France.
- 4 Service de Néphrologie-Transplantation, AP-HP, Hôpital Bicêtre, Le Kremlin-Bicêtre, France.
- 5 Service d'Explorations Fonctionnelles, AP-HP, Hôpital Necker Enfants Malades, Paris, France.
- 6 Service d'Explorations Fonctionnelles, AP-HP, Hôpital Européen Georges Pompidou, Paris, France.

Corresponding authors: Marco Pontoglio, PhD.

INSERM U1151 - CNRS UMR 8253 - Université de Paris
Team: Epigenetics and Development
Faculté de Médecine Necker
156-160 Rue de Vaugirard
75015 Paris, France
Email: marco.pontoglio@inserm.fr

Fabiola Terzi, MD, PhD.
INSERM U1151 - CNRS UMR 8253 - Université de Paris
Team: Mechanisms and Therapeutic Strategies of Chronic Kidney Disease
Faculté de Médecine Necker
156-160 Rue de Vaugirard
75015 Paris, France
Email: fabiola.terzi@inserm.fr

ABSTRACT

Kidney function is crucially dependent on the complex three-dimensional structure of nephrons. Any distortion of their shape may lead to kidney dysfunction. Traditional histological methods present major limitations for three-dimensional tissue reconstruction. Here, we combined tissue clearing, multi-photon microscopy and digital tracing for the reconstruction of single nephrons under physiological and pathological conditions. Sets of nephrons differing in location, shape and size according to their function were identified. Interestingly, nephrons tend to lie in planes. When this technique was applied to a model of cystic kidney disease, cysts were found to develop only in specific nephron segments. Along the same segment, cysts are contiguous within normal non-dilated tubules. Moreover, the shapes of cysts varied according to the nephron segment. Thus, our findings provide a valuable strategy for visualizing the complex structure of kidneys at the single nephron level and, more importantly, provide a basis for understanding pathological processes such as cystogenesis.

Key words: Tissue clearing / Kidney / Nephron / Cystic Kidney Disease / Nephronophthisis

TRANSLATIONAL STATEMENT

Clearing methods provide a unique tool for understanding how morphological changes lead to pathological consequences. Kidneys are critical organs that maintain body homeostasis through water, metabolite and electrolytes handling, which are crucially dependent on the complex three-dimensional (3D) structure of nephrons. When this structural organization is altered, renal pathophysiology ensues. In the present study, we have developed a powerful method based on optical clearing, multi-photon microscopy and digital tracing, for studying kidney at the single nephron level under physiological and pathological conditions. In particular, we provide the first 3D reconstruction of a polycystic kidney at the scale of single nephrons. This method can be applied to several pathological contexts allowing us to understand better the complex process of kidney deterioration and, consequently, to develop more targeted therapeutic strategies.

INTRODUCTION

Kidney maintains body homeostasis via its complex three-dimensional (3D) nephron structure. When this structural organization is altered, renal pathophysiology ensues. Chronic kidney diseases (CKD) are characterized by the development of renal lesions. Intriguingly, pathologists have reported a wide heterogeneity in the distribution of lesions during CKD^{1,2}. Whether this reflects the fact that specific nephron segments can be differently damaged, or alternatively, that some nephrons have different susceptibilities to be injured as a whole, is unknown. To address this issue, it is mandatory to reconstruct the 3D shape of nephrons in pathological contexts.

To the best of our knowledge, nephrons have only been fully reconstructed using serial 2D sections³⁻⁵. Although standard histological sectioning provides high resolution, 3D-reconstructions are very laborious and hard to obtain. This is primarily due to mechanical distortions, which is an inescapable effect of the slicing procedure. Furthermore, 3D-reconstruction from 2D images does not allow direct imaging of 3D structures in whole-mounted tissues.

Multiphoton microscopy has improved our ability to detect morphological changes in thick sections. However, a significant limitation is the shallow accessible depth due to light-scattering. By minimizing refractive index differences, clearing agents have dramatically improved the ability to image depths^{6,7}. Despite the fact that the first clearing agent was introduced a century ago⁸, it is only recently that several clearing protocols have been developed, mostly for brain⁹⁻¹⁷. Recent studies have demonstrated their potential for imaging other solid organs, such as liver, pancreas or kidney¹⁸⁻²⁶.

Polycystic kidney disease (PKD), a genetically heterogeneous disorder involving mutations in several ciliary genes, is the most common hereditary kidney disease^{27,28}. PKD is characterized by the development of cysts that lead to the complete destruction of the kidney²⁸.

Microdissection studies suggested that cysts can either develop as an “outpushing” of a nephron segment, as in autosomal dominant polycystic kidney disease (ADPKD); an ectatic expansion of collecting ducts, as in autosomal recessive polycystic kidney disease (ARPKD); or exclusively in medullary tubules, as in nephronophthisis (NPHP)^{27,29}. However, how cysts develop in 3D and organize with each other and normal neighboring tubules is still unknown. Here, we combined optical clearing with multiphoton microscopy to provide new insights into how nephrons are shaped and organized in physiological conditions and how they are modified during disease, such as cystogenesis. Our results demonstrate that there are three types of nephrons and that vessels may influence nephron spatial organization. Interestingly, we observed that nephrons tend to lie in specific planes. Unexpectedly, when we applied this technique to *jck* mice, we observed that cysts developed only in specific nephron segments with fusiform cysts intermingled with normal tubules.

RESULTS

Experimental setup

To study the shape of entire nephrons in relation to their environment, we adopted a technique based on optical clearing and multiphoton microscopy (**Supplementary Figure S1a**). By comparing different optical clearing protocols, we determined that, for kidney, Benzyl Alcohol/Benzyl Benzoate (BABB) was the most appropriate in term of efficacy (**Supplementary Figure S1b, S1c and Supplementary Table S1**).

3D-reconstruction and digital tracing requires high quality images with high resolution and high signal to background ratio (SBR). We observed that the optical signal provided by native fluorescence was not uniform over kidney sections. In particular, images from the medulla were poorly contrasted with a low SBR (**Supplementary Figure S2**). In order to improve the SBR, we stained sections with PAS (**Supplementary Figure 1d**), since we empirically noted that this staining gave rise to high contrast in thin sections during two-photon fluorescence. However, signal was not uniform throughout thick PAS-stained kidney sections (**Supplementary Figure 1e**). Therefore, we stained kidney sections with fluorochrome-coupled lectins: PNA and WGA, which stain glomeruli and tubules, and GSA, which marks blood vessels³⁰. Remarkably, with the combination of these lectins, SBR was dramatically increased in whole kidney sections with a significant improvement in both the xy-plane and z-axis (**Supplementary Figure 1e, Supplementary Movie S1**).

3D nephron segment visualization

In order to visualize the shape of whole nephrons, we traced their paths, beginning at the urinary pole of the glomerulus and ending at the collecting duct junction (**Supplementary Movie S2**). In spite of the fact that the lectins used globally bind all nephron segments, we noticed that when carefully inspected, these lectins were characterized by a specific pattern in the way they stained basal or luminal membranes in the different nephron segments. In other

words, we took advantage of the stereotypical pattern of lectin staining to identify the different nephron segments. In this way, we could easily identify six entities: proximal tubule (PT), thin limb (TL) of Henle loop (HL), thick ascending limb (TAL) of HL, distal convoluted tubule (DCT), connecting tubule (CNT) and collecting duct (CD). The transition between PT and TL was characterized by the sudden loss of the typical PT brush border signal and by the decrease of lumen width, which was almost virtually absent in TL (**Figure 1a**). Conversely, the transition between TL and TAL was characterized by a significant increase of external tubular diameter and relatively constant lumen width (**Figure 1b**). In all nephrons, the transition of TAL to DCT was systematically found at the vascular pole of the glomerulus. This transition was characterized by a sudden enlargement of external tubular diameter that was predominantly due to a significant increase of the lumen diameter (**Figure 1c**). The transition between DCT and CNT was characterized by a reduction of both the tubular diameter and lumen (**Figure 1d**). Finally, the connection between CNT and CCD was characterized by a sudden increase of both tubular diameter and lumen (**Figure 1e**). The quantification of these morphological transitions was statistically significant (**Figure 1f**) and its pertinence was verified with the staining with specific tubular markers (**Supplementary Figure S3, S4 and S5, and Supplementary Movie S3, S4 and S5**).

The shape and size of proximal tubules differ according to their depth

The staining of thick kidney sections allowed us to trace the coordinates of the spatial evolution of entire PT segments. Interestingly, we discovered that their shape was extremely variable and determined by the position of their glomeruli in the cortex. Globally, we identified three patterns. The first corresponded to the most superficial nephrons (SN, **Figure 2a, Supplementary Movie S6**), which occupied the most external part of the cortex (the most external 30% close to the renal capsule). Their convoluted parts formed compact structures with only 6-7 convolutions around their own glomerulus, occupying very small and tightly

packed spaces. The convolution of these SN ended in long and straight *pars recta* that descended into the medulla. At the opposite end of this spectrum, we observed a second pattern of nephrons located in the deepest part of the cortex (40% more internal depth), next to the medulla (juxtamedullary nephrons, JN, **Figure 2a**, **Supplementary Figure S6**, **Supplementary Movie S6**). Their PT were characterized by an initial short loop that systematically descended toward the papilla and then U-turned to ascend toward the renal capsule. In contrast to SN, JN proximal convoluted tubules were characterized by large coils that evolved around their own glomerulus and occupied large, loosely packed domains in the juxtamedullary cortex. The convoluted part of the PT of JN had 10-15 convolutions, forming large domains. Finally, the third pattern included nephrons located in the middle portion of the cortex (middle nephrons, MN, **Figure 2a**, **Supplementary Movie S6**). Interestingly, these tubules had a shape and spatial orientation that represented a transition between SN and JN. In fact, they contained 8-9 convolutions with coils that were larger than SN, but smaller than JN. In addition, MN had longer *pars recta* than JN. Interestingly, a global comparison of the shapes of the PT showed that SN and MN had a homogenous pattern whereas JN were extremely heterogeneous (**Supplementary Figure S6**). In addition, the spatial reconstruction of several nephrons revealed that PT never intermingle (**Supplementary Movie S6**), indicating that each nephron occupies its own individual space in the cortex.

Morphometric analyses confirmed the large differences in the size and shape of SN and JN, with an intermediate aspect for the MN. PT of JN were more than two-fold longer than the PT of SN (**Figure 2b**); however, the straightness was greater in SN compared to JN (**Figure 2c**), consistent with the observation that JN tubules were much more tortuous (**Figure 2a**, **Supplementary Figure S6**).

Glomerular size varies with depth

We then analyzed the depth and diameter of glomeruli randomly selected from each of the three zones. Morphometric analyses revealed that glomeruli were located in average 783 and 355 μm from the renal capsule in JN and SN, respectively. As previously reported, we observed that the size of glomeruli varied according to their depth. In particular, the glomerular volume of JN was three-times greater than that of SN and MN (**Figure 2d**).

3D-nephron reconstruction

We then traced the spatial evolution of entire nephrons from PT to CNT. The global view of their 3D-reconstruction confirmed that nephron shape differed among SN, MN and JN (**Figure 3a, Supplementary Movie S7**). This difference was mainly due to the structure of the PT. In addition, we also observed that HL had a different 3D spatial organization. In particular, the TL and TAL were more distantly separated in JN than in SN and MN (**Figure 3b**). Morphometric analyses revealed that JN were globally two-fold longer than SN (**Figure 3c**). The increased length was proportionally distributed in all segments, except for TAL and DCT which tended to have a similar absolute length in all nephron types (**Figure 3d**). This suggested that nephron elongation is a surprisingly homogeneously patterned process.

The arcuate vessels influence juxtamedullary proximal tubules convolution

To gain a more comprehensive perspective of kidney structure, we took advantage of GSA staining which allowed us to trace the arcuate vessels and their branches into the cortical radiate vessels (**Figure 4a and Supplementary Movie S8**). Interestingly, the concomitant 3D-reconstruction of nephrons and vessels showed that the arcuate vessels tend to be in a surprising parallel spatial organization with nearby tubules. In particular, we observed that the path followed by specific JN (constrained JN) tends to follow the path of the nearby vessel (**Figure 4b, Supplementary Movie S9**). Remarkably, this bias (observed only in a subset of JN nephrons) accounted for the large heterogeneity in the shapes of PT (**Supplementary**

Figure S6). Morphometric analyses revealed that the “constrained” PT were significantly longer and more tortuous (reduced straightness) than the “non-constrained” ones (**Figure 4c** and **4d**). It is worth noting that the convoluted parts of both SN and MN were positioned above the arcuate vessels and were not constrained.

Tubules tend to lie in planes

Interestingly, inspection of the 3D shapes of nephrons indicated that they tend to lie in planes (**Figure 5a, Supplementary Movie S10**). In order to quantify this parameter and to assess the possible statistical bias of this conformation, we measured the general tendency of tubules to bend out of the plane defined by their loops. Our measurements showed that, compared to a simulated model of random walking, generated with the same set of consecutive measured angles and length between consecutive points (**Figure 5b**), the tubules tended to evolve with smaller deviation from a plane (**Figure 5c**). This indicated that tubules tended to restrict their path along a plane. The observed differences were statistically highly significant ($P < 0.001$).

3D-nephron reconstruction reveals a specific pattern for cyst development

To determine whether our protocol allows for tracing nephrons in disorganized pathological tissues, we characterized the shapes and spatial distribution of cysts in *jck* mice, a widely-used model of nephronophthisis and cystic disease^{31–33}. 3D images showed that, in spite of the appearance of prominent cysts, the general 3D course of nephrons did not significantly differ from that of control mice (**Supplementary Movie S11**). Similarly, morphometric analyses confirmed that the global length of nephrons, glomerular volume and length of each nephron segment were comparable to those of control mice (**Supplementary Figure S7**). Of note, because of cyst development, we were unable to differentiate TL from TAL in HL. All the nephrons developed fusiform cysts (**Supplementary Movie S11 and S12**). One of the most striking features was the observation that fusiform cystic dilations occurred in multiple locations along the same nephron segment (**Supplementary Movie S12 and S13**).

Intriguingly, we observed that cysts never developed in PT and HL descending limbs (**Figure 6a, Supplementary Movie S12**). In contrast, they were predominantly detected in HL ascending limbs, DCT, CNT and in the upper part of CD, in continuity with CNT (**Figure 6a, Supplementary Movie S12**). In particular, we observed that HL, DCT as well as CNT segments had a peculiarly increased probability to develop cysts in their respective more distal parts (**Figure 6b**). Quantitative morphometric analyses on 3D-reconstruction images revealed that the total cyst volume per nephron was particularly high in CNT (**Figure 7a**). In addition, we observed that cyst enlargements in HL and DCT were greater in JN compared to SN and MN (**Figure 7a, Supplementary Movie S12**). Moreover, cyst incidence was significantly higher in JN compared to the other types of nephrons (**Figure 7b**). We also observed that the average glomerular inter-distance (calculated on the nearest 5 glomeruli) tended to be particularly increased in cystic mice, especially in the more superficial cortex (**Supplementary Figure S8**).

3D-reconstruction of numerous cysts revealed that they were extremely variable in shape and volume (**Figure 6c, Supplementary Movie S11 and S13**). In HL ascending limb, cysts had a fusiform shape with a small diameter. In DCT, cysts had a rather spherical and larger shape and were interspersed among non-dilated tubules. Interestingly, the transition between the DCT and CNT was systematically characterized by a normal non-dilated structure. In contrast, in CNT, we systematically observed a contiguous dilated cystic structure directly in contact with the CD. Interestingly, in CD, this structure progressively shrunk to a normal tubule size. More distally, no further cysts could be detected in the contiguous portion of the CD. Another consistent feature was the peculiar spatial organization of cysts in HL ascending limb. In fact, while cysts were deeper and closer to the loop in SN, they were more superficial and closer to DCT in JN (**Figure 6c**). Again, cysts occupied an intermediate position in MN (**Figure 6c**).

DISCUSSION

Traditional histological methods are limited in their ability to detect pathological changes that affect the global shape of nephrons. Here, we present a powerful approach based on tissue clearing that has the potential to address crucial questions in kidney architecture with unprecedented spatial detail in normal and pathological conditions. Our results confirmed the existence of three types of nephrons, which differ in their location, shape and size, consistent with their functional specificities. Moreover, we demonstrated that nephrons tend to lie in planes and to adapt to vessel spatial organization. Intriguingly, when we applied this technique to a model of cystic kidney disease, we observed that cysts develop in all nephrons, but only in specific segments. Interestingly, we showed that cyst shape varies according to the nephron segment, and that along the same nephron, cysts intercalate with normal non-dilated tubules. Altogether, these results provide the first 3D-characterization of the spatial arrangement of nephrons and vessels and importantly provide the basis for understanding a pathological process, such as cystogenesis.

Kidney optical clearing is challenging due to high levels of autofluorescence and cell density. By comparing different clearing protocols, we identified in BABB a powerful technique for implementing the visualization and reconstruction of structures located in the deepest part of the kidney, i.e. the medulla. Moreover, BABB is rapid and scalable and, once cleared, samples can be stored for months before image acquisition. Another main advantage of this technique is its low cost. Clearing agents may result in shrinking or enlargement of structures⁹⁻¹⁷. However, since these modifications of kidney size are isotropic, the relative measurements are not expected to be affected or bias their interpretation. One of the most important limitations is the annotation of structures that is highly time-consuming. Nevertheless, there is a growing number of techniques based on deep learning that should rapidly overcome this limitation.

Consistent with the results obtained by classical techniques, our study showed that nephrons differ in their shape and length according to their position. In particular, we observed that JN have more developed convoluted proximal tubules, larger glomeruli and are two-times longer than SN. The increased length is the result of a harmonious process since lengthening affects proportionally all nephron segments. We also observed that JN have larger HL. Altogether these data clearly show that the microanatomy of SN and JN is significantly different and that the MN display intermediate features. Interestingly, physiological studies have shown that nephrons are also functionally different². The morphogenetic events that underlie these differences are not yet known. It is thus tempting to speculate that the particular structure of JN may account for the specificity of their functions.

Interestingly, by providing for the first time the 3D-reconstruction of nephrons and their surrounding vessels, we discovered a spatial constraint between the arcuate vessels and a subgroup of nephrons. Thus, it is conceivable to think that vessels may dictate the way nephrons lengthen during development^{34,35}. The inspection of the 3D shapes of nephrons combined with computational simulations also revealed that nephrons never intermingle and that each nephron tends to lie in a plane. The functional significance of this observation remains to be elucidated.

Cyst development during PKD is still an intriguing process. NPHP, a pathological condition characterized by cyst development, is the most common genetic disease-causing end-stage renal disease in children and adolescents. Twenty NPHP genes have been identified so far³⁶. Among them, *NEK8* encodes a member of the NIMA (never in mitosis A)-related kinase family which plays a role in cilia function and cell cycle progression³⁷. *Nek8* was originally characterized as the gene mutated in *jck* mice³². Notably, a mutation in the same protein domain has been shown to lead to NPHP9 in humans³⁸. 2D studies suggested that cyst

development dramatically differs among the different forms of PKD^{27,29}. In particular, in NPHP, cysts seem to be derived exclusively from CD and DCT³¹. Although informative, these immunohistochemical studies cannot argue against the possibility that the loss of specific tubular markers³⁹ artificially accounts for this observation. Thus, our 3D study provides the first clear evidence that cyst development is a process that may involve only specific nephron segments. Interestingly, while NEK8 is expressed in the cytoplasm of all nephron segments, its expression in cilia is restricted to DCT and CD. Since these segments are the only prone to develop cysts³¹, we can postulate that the disruption of NEK8 ciliary function is the crucial event for cyst formation. Intriguingly, we also observed that fusiform cysts are in continuity with normal non-dilated tubules. The fact that a recessive germ-line mutation leads to a pathological phenotype in only a subset of cells suggests that a second event might trigger cyst development in these cells, as suggested for ADPKD^{40,41}.

We also observed that cyst enlargement is more predominant in JN compared to SN, at least considering the cysts that locate between PT and CNT. Consistently, it has been reported that in the context of glomerulosclerosis, glomerular lesions are found more frequently in JN than in SN^{1,21,42}. Whether the overwork due to the increased single nephron glomerular filtration rates and transport/enzymatic activities accounts for the increased susceptibility of JN to deteriorate is an interesting hypothesis that deserves further investigations.

In summary, we describe a new technique to image kidneys in 3D with sufficient molecular specificity and resolution to directly record the spatial and quantitative distribution of specifically labeled internal structures (nephrons, vessels, cysts). Given the convenience, speed and ability for direct quantification, we anticipate that this technique will become a powerful tool for understanding kidney pathophysiology.

MATERIEL AND METHODS

Animals

All animal procedures were approved by the “Services Vétérinaires de la Préfecture de Police de Paris” and by the ethical committee of Université Paris Descartes. Two-month-old FVB/N mice (n=20) were used for setting up the clearing conditions. The study was then conducted on 2-week-old *jck* male mice (n=4) and control littermates (n=3).

Preparation of renal tissues

Before sacrifice, mice were perfused, via intracardiac catheterization, with 25 ml of heparinized saline (1000 IU/L) followed by 75 ml of 4% paraformaldehyde (PFA) in PBS. Experiments were performed under xylazine (Rompun 2%; Bayer; 6 µg/g of body weight) and ketamine (Clorketam 1000; Vetoquinol SA; 120 µg/g of body weight) anesthesia.

For clearing studies, kidneys were fixed in 4% PFA for 4 hours, embedded in 4% agarose, and 1.5-mm thick sections surrounding the renal hilum were cut and stored in PBS at 4°C. Kidney sections were first stained and then cleared.

For immunohistochemical studies on thin sections, kidneys were fixed in 4% PFA overnight, paraffin-embedded, and 4-µm sections were cut.

Staining

PAS staining

The 1.5-mm kidney sections were incubated in pure or 1:100 PBS-diluted PAS for 5 minutes at room temperature before clearing.

Immunohistochemistry on thin paraffin-embedded sections

4-µm sections of paraffin-embedded kidneys were heated for antigen retrieval and incubated overnight at 4°C with fluorochrome-coupled lectins in order to trace the tubules (Rhodamine Peanut Agglutinin [PNA; RL-1072-5] and Rhodamine Wheat Germ Agglutinin [WGA; RL-1022-5], Vector Laboratories, diluted at 1/200) and segment-specific primary antibody in

order to depict distinct tubular segments (Biotinylated Lotus Tetragonolobus Lectin [LTL; B-1325], Vector Laboratories, diluted at 1/1 00; mouse anti-Calbindin D28K [D-4], Santa Cruz, diluted at 1/200; goat anti-AQP2 [C-17], Santa Cruz, diluted at 1/200). The next day, the sections were incubated with the secondary antibody for 1 h at room temperature (Alexa Fluor 488 Conjugate, [S32354], Invitrogen; anti-Goat/Alexa Fluor 488 [A-11055], Invitrogen; anti-Mouse/Alexa Fluor 488 [A-21202], Invitrogen; all diluted at 1/500) before being colored with DAPI. All images were acquired with a Nikon Eclipse E800 Microscope and prepared using FiJi Software.

Lectin staining on thick sections

The 1.5-mm thick kidney sections were incubated at 4°C for 1 month in Texas Red or Fluorescein-Isothiocyanate-coupled lectins: PNA [RL-1072-5] and WGA [RL-1022-5], diluted at 1/100 in 0.1% PBS azide and 0.1% Triton-X. Sections were then washed every day for 2 weeks with PBS before clearing.

Optical clearing

For Scale clearing, 1.5-mm kidney sections were incubated in ScaleA2 (4M Urea, 0.1% Triton X-100, 10% Glycerol) or ScaleB4 (8M Urea, 0.1% Triton X-100) for 2 weeks, up to 1 year, at 4°C.

For BABB clearing, 1.5-mm kidney sections were dehydrated in sequential rinses of EtOH at room temperature. The samples were then incubated in BABB (Sigma-Aldrich) in a 1:2 ratio for at least 2 days at 4°C.

Two-photon microscopy images acquisition

Tissues were imaged with aqueous gel an inverted multiphoton microscope (Lavision Biotec) equipped with a Mai Tai HP Titanium-Sapphire laser (Spectra-Physics) (**Supplementary Figure S1a**). The excitation wavelength was 815 nm at 8% of power. We used a 20X water immersion objective (XLUMPLFL20XW, Olympus), N.A. 0.95, W.D. 2.0 mm. For

fluorescence acquisition, we used a Non-Descanned Detector at 80% with a bandpass filter 593/40nm.

The first step consisted in 2D mosaic image acquisition at the middle z-stack using suboptimal acquisition parameters (400- μm X 400- μm and 1011 X 1011 pixels, with 10% overlap and a line averaging at 2) in order to guide the selection of the most relevant central fields (**Supplementary Figure S9a**). Once the xy grid and z fields of interest were defined, parameters were adjusted to acquire high quality images. Such approach reduced the region of interest to 5 x 12 fields per z-stack. Then, we acquired 850 z-stacks/optical slices (1- μm step size) surrounding the renal hilum in the middle part of the kidney section.

Image stitching, processing and tracing

Each stack was tiled according to the method developed by Preibisch et al.⁴³, which allows the stitching of a large collection of images by using the "Grid/Collection stitching" plugin of the Fiji software (<http://fiji.sc/Fiji>). Since we observed an important shift between two adjacent images after stitching, we wrote a custom-matching program in Python. This program compensates the image shift allowing us to correctly align the images (**Supplementary Figure S9b**). Stitched-corrected images were analyzed using Imaris (Version 8.4.2, Bitplane). Tubules and vessels were traced using the filament tracer package manual mode of Imaris and joined by an Imaris Xtension that we developed on Matlab (https://www.dropbox.com/s/sm9u5em3orjrpnc/Standalone_Join_Filament_Tool.zip?dl=0) (**Supplementary Figure S9c**). Glomeruli and cysts were 3D-reconstructed using the manual mode of the surface package of Imaris. The 3D glomeruli spatial organization was displayed using the manual mode of the spots package of Imaris.

Morphometry

Tubular segment length, nephron length and straightness were determined using the filament tracer package of Imaris. According to the Imaris Software, the straightness was quantified as

the ratio between the distance between two points and the length of the nephron segment path. 31 PT and 12 whole nephrons were reconstructed and measured in 3 wild-type mice whereas 37 PT and 17 whole nephrons were reconstructed and measured in 4 *jck* mice. Cyst and glomerular volumes were determined using the “surface package” of Imaris. 31 and 34 glomeruli were measured in wild-type and *jck* mice, respectively. 74 cysts were measured in total.

The “out of the plane” angles of tubular turns (indicated as “Beta”) were measured between the plane (defined by three consecutive points) and the direction with the next consecutive fourth point in space (**Figure 5b**). To evaluate the statistical significance of the observed bias, we simulated the distribution of Beta angles with a random rotation of Beta angles (Monte Carlo simulation) in structures that were composed by the same segments with the same set of alpha angles.

For the calculation of the probability to develop a cystic lesion along nephron segments, we represented each nephron by a set of points in space. Each point was annotated in respect for the presence of cyst *vs* normal structure and the type of segment. The probability at each standardized length (set to 50 bins) was calculated as the ratio between the numbers of points with cystic annotation and the total number of points in the bin.

For the calculation of the average glomerular inter-distance, we considered for each glomerulus the average glomerular inter-distance calculated on the nearest 5 glomeruli.

Data analyses and statistics

Data are expressed as the mean \pm S.E.M. Differences between the experimental groups were evaluated using ANOVA followed, when significant ($P < 0.05$), by the Tukey-Kramer test. When only two groups were compared, the Mann-Whitney test was used. Statistical analyses were performed using Graph Prism Software.

DISCLOSURE STATEMENT

The authors declare that they have no conflict of interest.

REFERENCES

1. Rich AR. A hitherto undescribed vulnerability of the juxtamedullary glomeruli in lipid nephrosis. *Bull Johns Hopkins Hosp.* 1957;100(4):173-186.
2. Bankir L, Bouby N, Trinh-Trang-Tan MM. Heterogeneity of nephron anatomy. *Kidney Int Suppl.* 1987;20:S25-39.
3. Christensen EI, Grann B, Kristoffersen IB, Skriver E, Thomsen JS, Andreassen A. Three-dimensional reconstruction of the rat nephron. *Am J Physiol Physiol.* 2014;306(6):F664-F671.
4. Zhai XY, Birn H, Jensen KB, Thomsen JS, Andreassen A, Christensen EI. Digital three-dimensional reconstruction and ultrastructure of the mouse proximal tubule. *J Am Soc Nephrol.* 2003;14(3):611-619.
5. Zhai X-Y, Thomsen JS, Birn H, Kristoffersen IB, Andreassen A, Christensen EI. Three-Dimensional Reconstruction of the Mouse Nephron. *J Am Soc Nephrol.* 2006;17(1):77-88.
6. Puelles VG, Moeller MJ, Bertram JF. We can see clearly now: Optical clearing and kidney morphometrics. *Curr Opin Nephrol Hypertens.* 2017;26(3):179-186.
7. Seo J, Choe M, Kim S-Y. Clearing and Labeling Techniques for Large-Scale Biological Tissues. *Mol Cells.* 2016;39(6):439-446.
8. Spalteholz W. Über das Durchsichtigmachen von menschlichen und tierischen Präparaten. *Leipzig S Hierzel.* 1914.
9. Hama H, Kurokawa H, Kawano H, et al. Scale: A chemical approach for fluorescence imaging and reconstruction of transparent mouse brain. *Nat Neurosci.* 2011;14(11):1481-1488.
10. Ertürk A, Becker K, Jährling N, et al. Three-dimensional imaging of solvent-cleared

- organs using 3DISCO. *Nat Protoc.* 2012;7(11):1983-1995.
11. Kuwajima T, Sitko AA, Bhansali P, Jurgens C, Guido W, Mason C. ClearT: a detergent- and solvent-free clearing method for neuronal and non-neuronal tissue. *Development.* 2013;140(6):1364-1368.
 12. Ke MT, Imai T. Optical clearing of fixed brain samples using SeeDB. *Curr Protoc Neurosci.* 2014;(SUPPL.66):1-19.
 13. Chung K, Deisseroth K. CLARITY for mapping the nervous system. *Nat Methods.* 2013;10(6):508-513.
 14. Tomer R, Ye L, Hsueh B, Deisseroth K. Advanced CLARITY for rapid and high-resolution imaging of intact tissues. *Nat Protoc.* 2014;9(7):1682-1697.
 15. Yang B, Treweek JB, Kulkarni RP, et al. Single-cell phenotyping within transparent intact tissue through whole-body clearing. *Cell.* 2014;158(4):945-958.
 16. Susaki EA, Tainaka K, Perrin D, et al. Whole-brain imaging with single-cell resolution using chemical cocktails and computational analysis. *Cell.* 2014;157(3):726-739.
 17. Alanentalo T, Asayesh A, Morrison H, et al. Tomographic molecular imaging and 3D quantification within adult mouse organs. *Nat Methods.* 2007;4(1):31-33.
 18. Parra SG, Chia TH, Zinter JP, et al. Multiphoton microscopy of cleared mouse organs. *J Biomed Opt.* 2010; 15:036017
 19. Renier N, Wu Z, Simon DJ, et al. iDISCO: a simple, rapid method to immunolabel large tissue samples for volume imaging. *Cell* 2014;159:896–910.
 20. Lee H, Park JH, Seo I, Park SH, Kim S. Improved application of the electrophoretic tissue clearing technology, CLARITY, to intact solid organs including brain, pancreas, liver, kidney, lung, and intestine. *BMC Dev Biol.* 2014;14(1):1-7.
 21. Iversen BM, Amann K, Kvam FI, Wang X, Ofstad J. Increased glomerular capillary pressure and size mediate glomerulosclerosis in SHR juxtamedullary cortex. *Am J*

- Physiol Physiol.* 1998;274(2):F365-F373.
22. Angelotti ML, Antonelli G, Conte C, Romagnani P. Imaging the kidney: from light to super-resolution microscopy. *Nephrol Dial Transplant.* July 2019.
 23. Puelles VG, van der Wolde JW, Schulze KE, et al. Validation of a Three-Dimensional Method for Counting and Sizing Podocytes in Whole Glomeruli. *J Am Soc Nephrol.* 2016;27(10):3093-3104.
 24. Pannabecker TL, Dantzler WH, Layton HE, Layton AT. Role of three-dimensional architecture in the urine concentrating mechanism of the rat renal inner medulla. *Am J Physiol Physiol.* 2008;295(5):F1271-F1285.
 25. Saritas T, Puelles VG, Su X-T, McCormick JA, Welling PA, Ellison DH. Optical Clearing in the Kidney Reveals Potassium-Mediated Tubule Remodeling. *Cell Rep.* 2018;25(10):2668-2675.e3.
 26. Schuh CD, Polesel M, Platonova E, et al. Combined structural and functional imaging of the kidney reveals major axial differences in proximal tubule endocytosis. *J Am Soc Nephrol.* 2018;29(11):2696-2712.
 27. Braun DA, Hildebrandt F. Ciliopathies. *Cold Spring Harb Perspect Biol.* 2017;9(3):a028191.
 28. Bergmann C, Guay-Woodford LM, Harris PC, Horie S, Peters DJM, Torres VE. Polycystic kidney disease. *Nat Rev Dis Prim.* 2018;4(1):50.
 29. Wilson PD. Polycystic kidney disease. *N Engl J Med.* 2004;350(2):151-164.
 30. Laitinen L, Virtanen I, Saxén L. Changes in the glycosylation pattern during embryonic development of mouse kidney as revealed with lectin conjugates. *J Histochem Cytochem.* 1987;35(1):55-65.
 31. Smith LA, Bukanov NO, Husson H, et al. Development of Polycystic Kidney Disease in Juvenile Cystic Kidney Mice: Insights into Pathogenesis, Ciliary Abnormalities, and

- Common Features with Human Disease. *J Am Soc Nephrol*. 2006;17(10):2821-2831.
32. Liu S, Lu W, Obara T, et al. A defect in a novel Nek-family kinase causes cystic kidney disease in the mouse and in zebrafish. *Development*. 2002;129(24):5839-5846.
 33. Franke M, Baeßler B, Vechtel J, et al. Magnetic resonance T2 mapping and diffusion-weighted imaging for early detection of cystogenesis and response to therapy in a mouse model of polycystic kidney disease. *Kidney Int*. 2017;92(6):1544-1554.
 34. Barry DM, McMillan EA, Kunar B, et al. Molecular determinants of nephron vascular specialization in the kidney. *Nat Commun*. 2019;10(1).
 35. Perretta-Tejedor N, Jafree DJ, Long DA. Endothelial-epithelial communication in polycystic kidney disease: Role of vascular endothelial growth factor signalling. *Cell Signal*. 2020;72.
 36. Srivastava S, Molinari E, Raman S, Sayer JA. Many Genes-One Disease? Genetics of Nephronophthisis (NPHP) and NPHP-Associated Disorders. *Front Pediatr*. 2017;5:287.
 37. Fry AM, O'Regan L, Sabir SR, Bayliss R. Cell cycle regulation by the NEK family of protein kinases. *J Cell Sci*. 2012;125(19):4423-4433.
 38. Otto EA, Trapp ML, Schultheiss UT, Helou J, Quarmby LM, Hildebrandt F. NEK8 mutations affect ciliary and centrosomal localization and may cause nephronophthisis. *J Am Soc Nephrol*. 2008;19(3):587-592.
 39. Wilson PD. Apico-basal polarity in polycystic kidney disease epithelia. *Biochim Biophys Acta*. 2011;1812(10):1239-1248.
 40. Happé H, Leonhard WN, van der Wal A, et al. Toxic tubular injury in kidneys from Pkd1-deletion mice accelerates cystogenesis accompanied by dysregulated planar cell polarity and canonical Wnt signaling pathways. *Hum Mol Genet*. 2009;18(14):2532-2542.
 41. Piontek K, Menezes LF, Garcia-Gonzalez MA, Huso DL, Germino GG. A critical

developmental switch defines the kinetics of kidney cyst formation after loss of Pkd1. *Nat Med.* 2007;13(12):1490-1495.

42. Ikoma M, Yoshioka T, Ichikawa I, Fogo A. Mechanism of the unique susceptibility of deep cortical glomeruli of maturing kidneys to severe focal glomerular sclerosis. *Pediatr Res.* 1990;28(3):270-276.
43. Preibisch S, Saalfeld S, Tomancak P. Globally optimal stitching of tiled 3D microscopic image acquisitions. *Bioinformatics.* 2009;25(11):1463-1465.

ACKNOWLEDGMENTS

We thank the LEAT, Histology and Imaging Platforms of Structure Federative de Recherche Necker for technical assistance. We thank Pierre Isnard, Marie-Claire Gubler and Nicolas Kuperwasser for critical reading of the manuscript. This work was supported by Institut National de la Santé et de la Recherche Médicale, Université Paris Descartes, Assistance Publique Hôpitaux de Paris, Agence Nationale Recherche, Whoami Laboratoire d'Excellence, Pharma Research and Early Development Roche Laboratories (Basel, Switzerland) and Institut Roche de Recherche et Médecine Translationnelle (Paris, France).

AUTHOR CONTRIBUTIONS

T.B., N.G. and M.Z. designed, performed experiments and analyzed the data. F.B., L.T., M.G.T. and S.G. also performed some experiments and analyzed the data. M.B. and C.N. performed the mouse experiments. T.B. and M.Z. also contributed to writing the manuscript. B.K. and G.F. revised the manuscript. F.T. and M.P. provided the conceptual framework and designed the study, supervised the project and wrote the paper.

FIGURE LEGEND

Figure 1: Morphological criteria used to identify nephron segments. (a-e) Morphology of the different segments of the nephron in control mice. Nephrons were traced from the urinary pole of the glomerulus to the collecting duct (PT, proximal tubule: turquoise, TL, thin limb of Henle loop: light grey, TAL, thick ascending limb of Henle loop: dark grey, DCT, distal convoluted tubule: pink, CNT, connecting tubule: yellow, CCD, cortical collecting duct: orange). The arrows illustrate the diameter of the different nephron segments. (f) Quantification of the outer tubular diameter of the different nephron segments. All data are shown as means \pm S.E.M. Analysis of variance (ANOVA) followed by Tukey-Kramer test: ** $P < 0.01$, *** $P < 0.001$.

Figure 2: 3D proximal tubule reconstruction reveals three different shapes and organization. (a) Representative 3D reconstruction images of proximal tubules through the entire renal cortex, divided into three levels (white lines) according to the shape of proximal tubules (PT): superficial (blue), middle (green) and juxtamedullary (red) cortex, corresponding to the outer 30%, middle 30%, and inner 40% of the cortex, respectively. (Scale bar, 150 μ m). Note the different shape of the three types of nephrons and in particular the length and tortuosity of the juxtamedullary tubules. (b-c) Quantification of the (b) length and (c) straightness of the 3 types of proximal tubules. (d) Quantification of the volume of glomeruli from each cortex region. All data are shown as means \pm S.E.M. Analysis of variance (ANOVA) followed by Tukey-Kramer test: juxtamedullary PT *versus* superficial PT: ### $P < 0.001$; juxtamedullary PT *versus* middle PT: *** $P < 0.001$; superficial PT *versus* middle PT: \$\$\$ $P < 0.001$.

Figure 3: 3D nephron reconstruction reveals three different types of nephrons. (a) Representative 3D images of a whole nephron (left panels) from glomeruli to collecting duct in superficial cortex (blue), middle cortex (green) and juxtamedullary region (red) in control

mice. Nephron segmentation (right panels) for the three different types of nephrons. (Scale bar, 150 μm). **(b)** Quantification of the inter-distance between the 2 limbs of the Henle loop for the 3 types of nephrons. **(c)** Quantification of nephron length for the 3 types of nephrons. **(d)** Quantification of the length of the different segments of the nephron according to the type of nephron. All data are shown as means \pm S.E.M. Analysis of variance (ANOVA) followed by Tukey-Kramer test: JN *versus* SN: ### $P < 0.001$; JN *versus* MN: * $P < 0.05$, ** $P < 0.01$, *** $P < 0.001$.

Figure 4: Vessels determine nephron shape. **(a)** 3D reconstruction of vessel architecture from the arcuate vessels to the cortical radiate vessels. (Scale bar, 200 μm). **(b)** Representative images of “non-constrained” (upper panel) and “constrained” (lower panel) juxtamedullary proximal tubules. (Scale bar, 100 μm). **(c-d)** Quantification of the **(c)** length and **(d)** straightness of “non-constrained” and “constrained” juxtamedullary proximal tubules. All data are shown as means \pm S.E.M. Mann-Whitney test: “constrained” *versus* “non-constrained”: * $P < 0.05$, *** $P < 0.001$.

Figure 5: Nephron tubules tend to evolve as a flat structure. **(a)** A typical path of a nephron proximal tubule. This path illustrates its tendency to lie on a plane. The planarity of the evolution of the path can be better seen when properly rotated and aligned with the observer point of view (see the right-hand representation of the same tubular segment which, on the left-hand side, is represented on a different angle). **(b)** Schematic representation of a tubular path composed of 4 segments (between 5 points defining a given tubular path shown as an example). The degree to which paths tend to go “out of their plane” can be represented by the angle indicated here as “beta”. This angle is measured between the segment p_3-p_4 in respect to the plane (defined by the immediately preceding points p_3 , p_2 and p_1) and represented by a dark grey rectangle in the scheme. Calculation of beta angles was then recursively calculated all along the set of points in a tubular path. To evaluate the extent of the

bias of these beta angles we simulated a random walking (Monte Carlo simulation, MCs) by using the same set of consecutive alpha angles of each tubular path (measured between all consecutive segments). This random walking generated path with an identical set of alpha angles and randomized beta angles. (c) Violin-Plots of global distribution of beta angles and the result of a Monte Carlo simulation (MCs) in PT, Proximal Tubules; TL, Thin Limb of Henle loop; TAL, Thick Ascending Limb of Henle loop; DCT, Distal Convoluted Tubule and CNT, Connective Tubules. Monte Carlo Simulation, $P < 0.001$.

Figure 6: 3D nephron reconstruction reveals that cysts develop only in specific nephron segments. (a) Representative 3D images with cyst volume rendering of a whole nephron (left panels) from glomeruli to collecting duct in superficial cortex (blue), middle cortex (green) and juxtamedullary region (red) in *jck* mice. Nephron segmentation (right panels) for the three different types of nephrons. (Scale bar, 150 μm). (b) Probability to develop cysts in the different nephron segments in *jck* mice. The horizontal axis is a normalized length of nephrons corresponding to 50 bins (PT: proximal tubule, turquoise; HL: Henle's Loop, white; DCT: distal convoluted tubule, pink; CNT: connecting tubule, yellow). (c) Representative 3D cysts reconstruction images with cyst volume rendering of ascending limb of the Henle loop (left panels), distal convoluted tubules (middle panels), connecting tubule and collecting ducts ((right panels) in superficial (upper panels), middle (middle panels) and juxtamedullary (lower panels) nephrons in *jck* mice. (Scale bar, 50 μm).

Figure 7: Characterization of cyst distribution and volume throughout the nephron. (a) Quantification of the total cyst volume (sum of the cysts per nephron) for each nephron segment (HL: Henle's loop, white; DCT: distal convoluted tubule, pink; CNT: connecting tubule, yellow) and (b) length of tubule occupied by the cysts for each type of nephron (superficial: blue; middle: green; juxtamedullary: red) in *jck* mice. All data are shown as

means \pm S.E.M. Analysis of variance (ANOVA) followed by Tukey-Kramer test: JN *versus* SN: # P < 0.05; JN *versus* MN: * P < 0.05, ** P < 0.01.

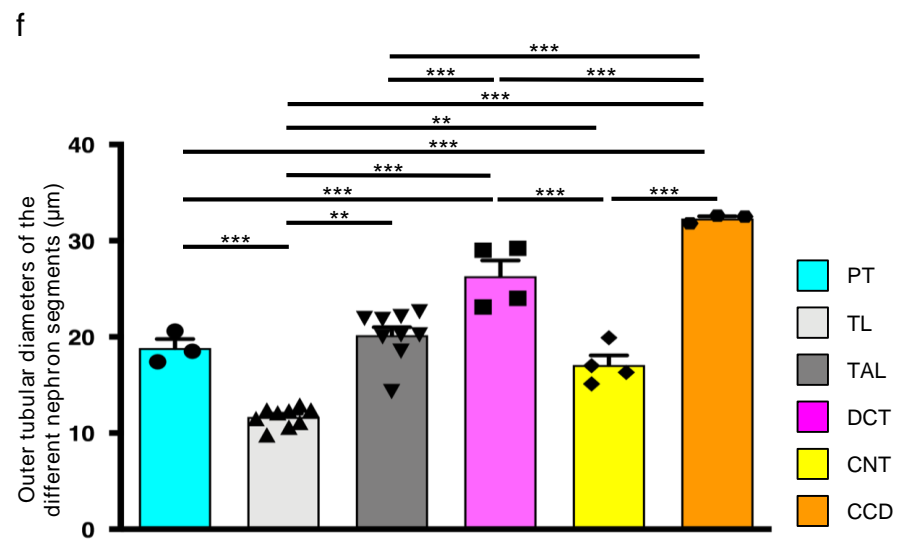
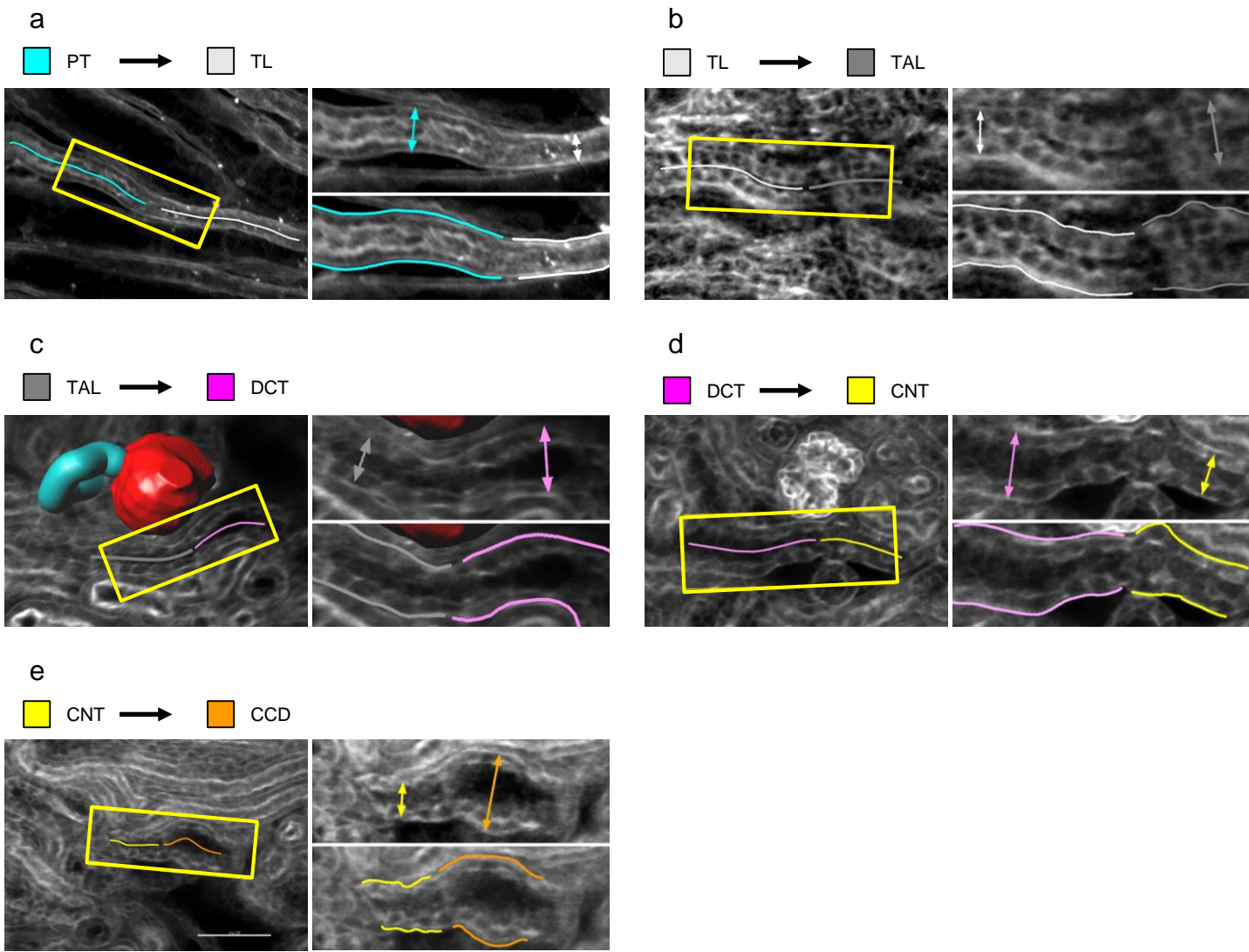
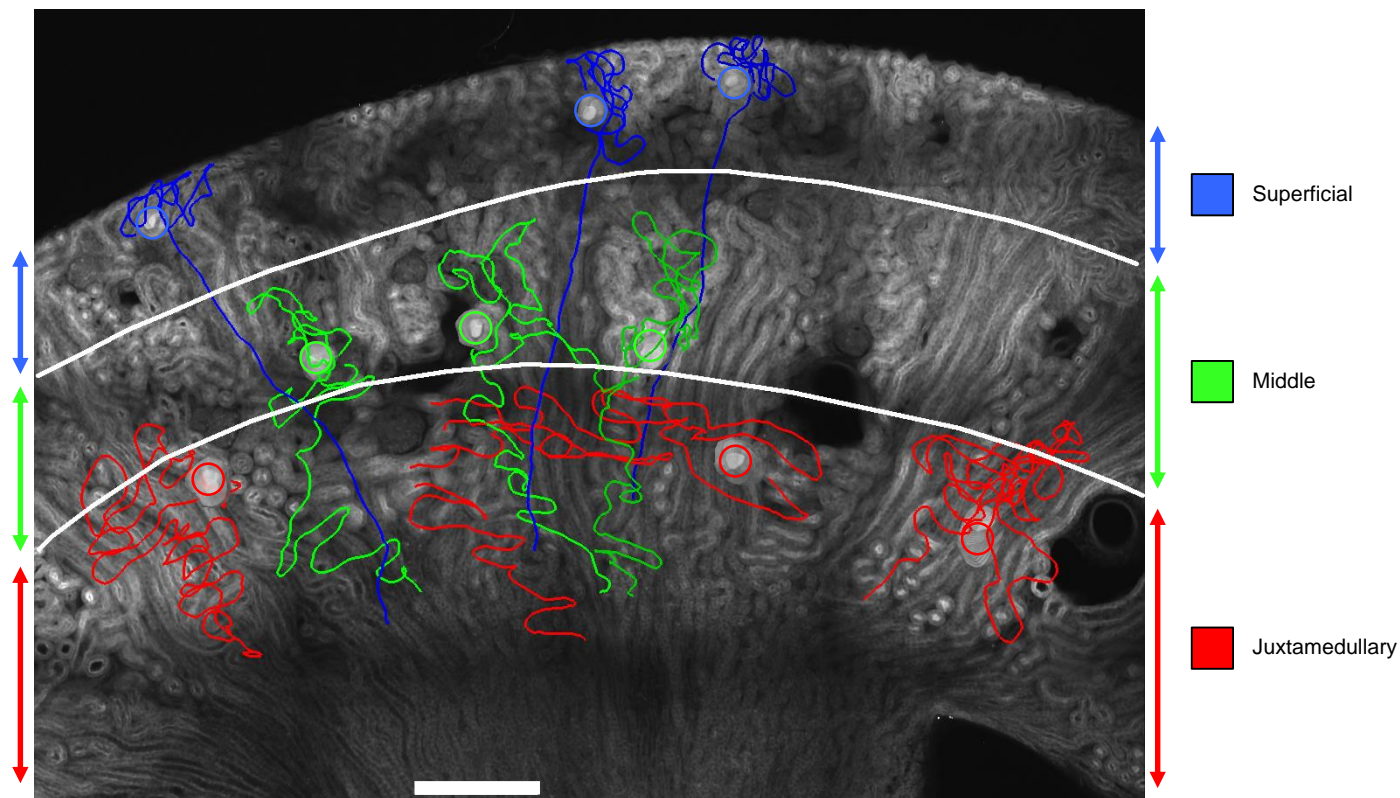
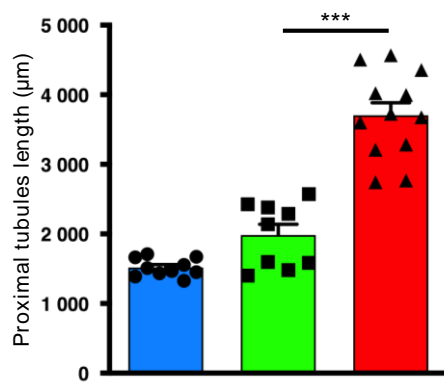


Figure 1

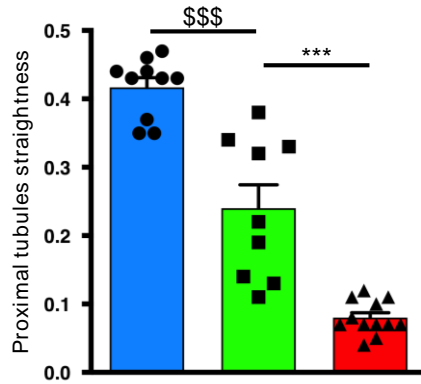
a



b



c



d

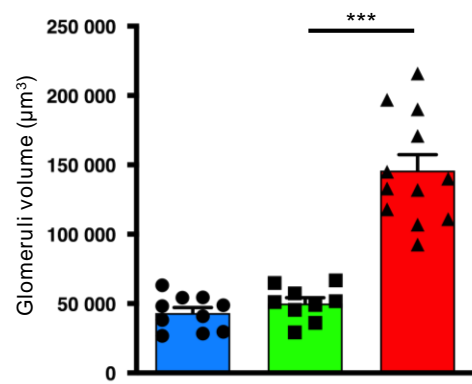


Figure 2

a

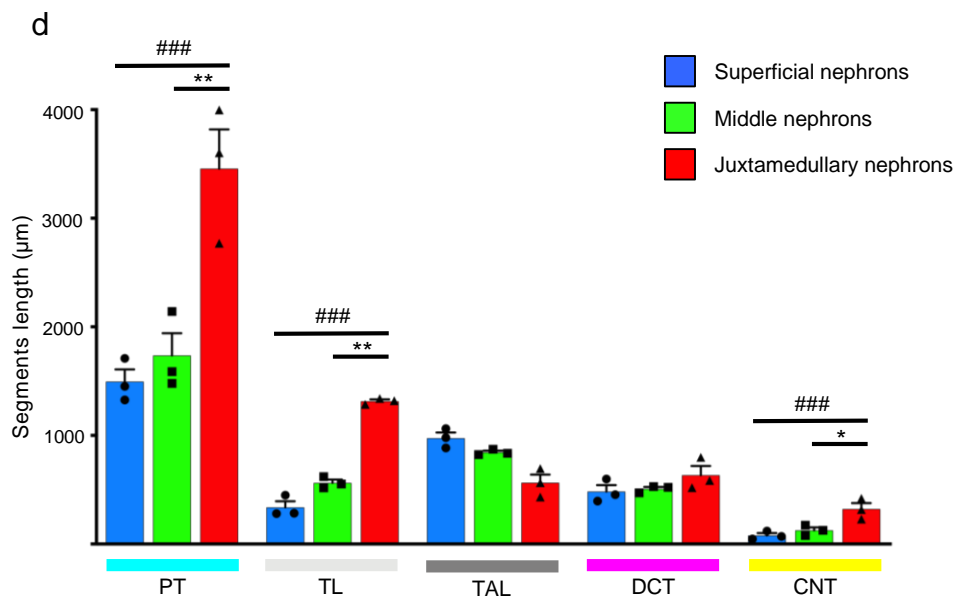
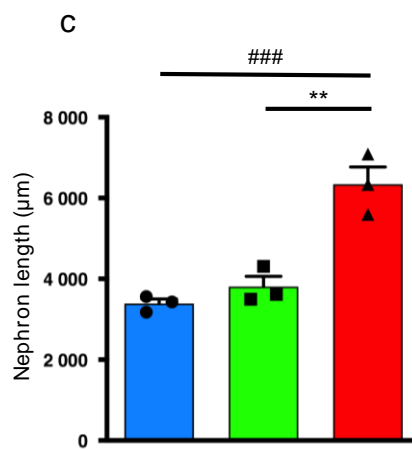
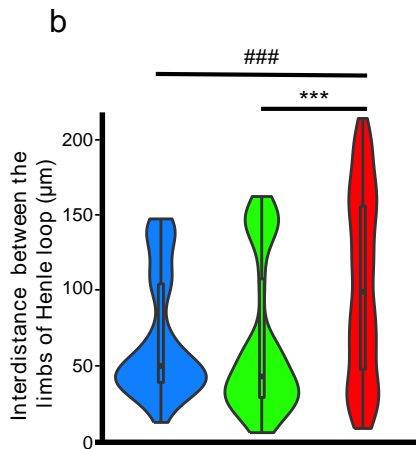
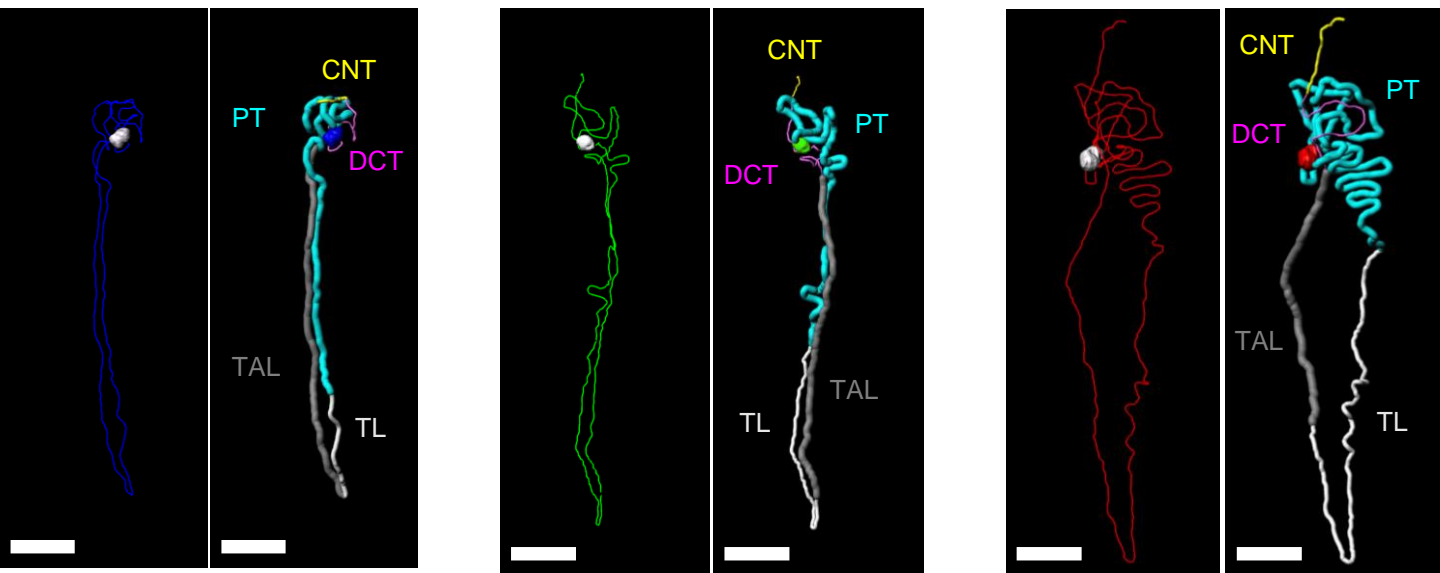


Figure 3

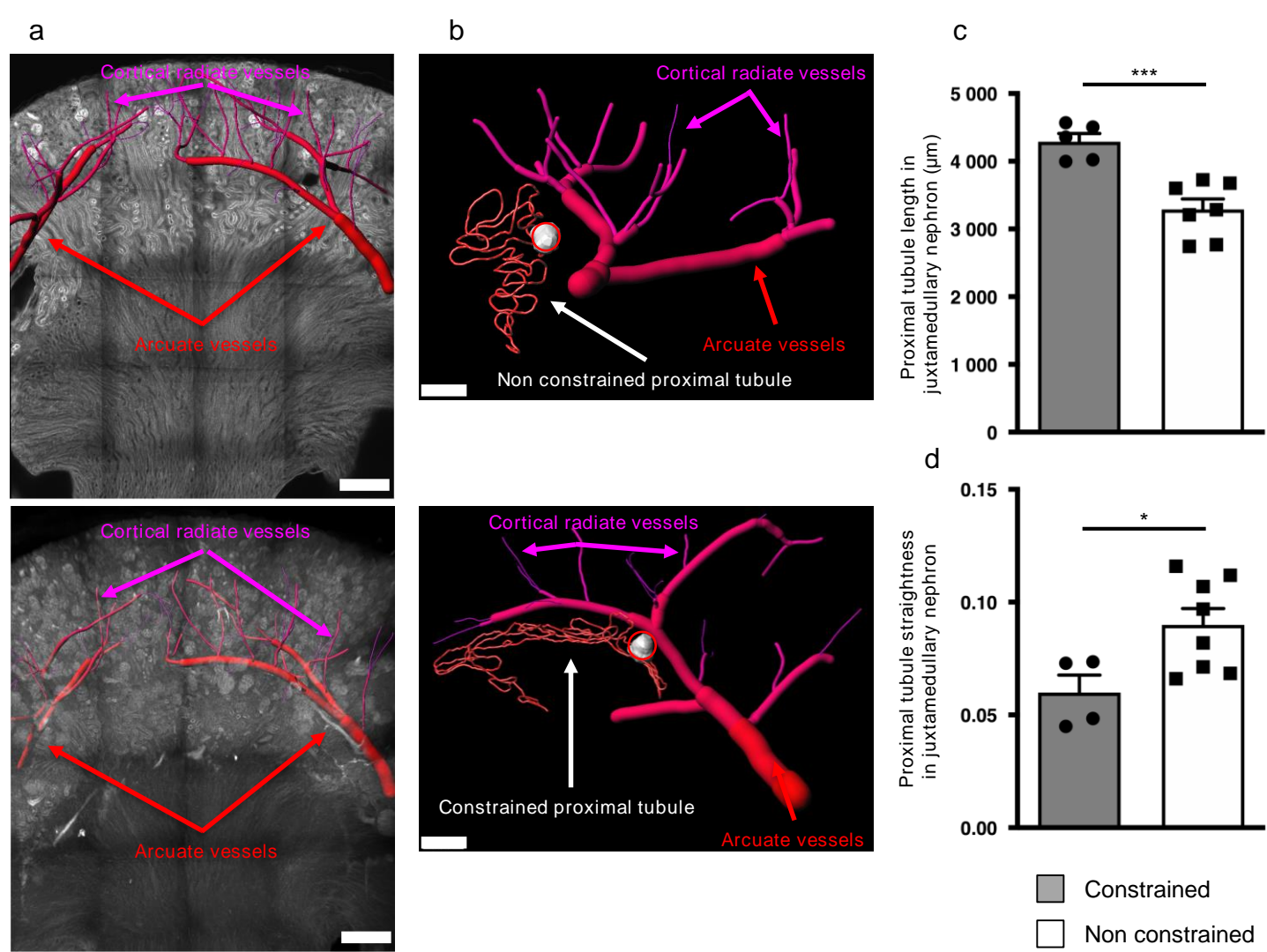
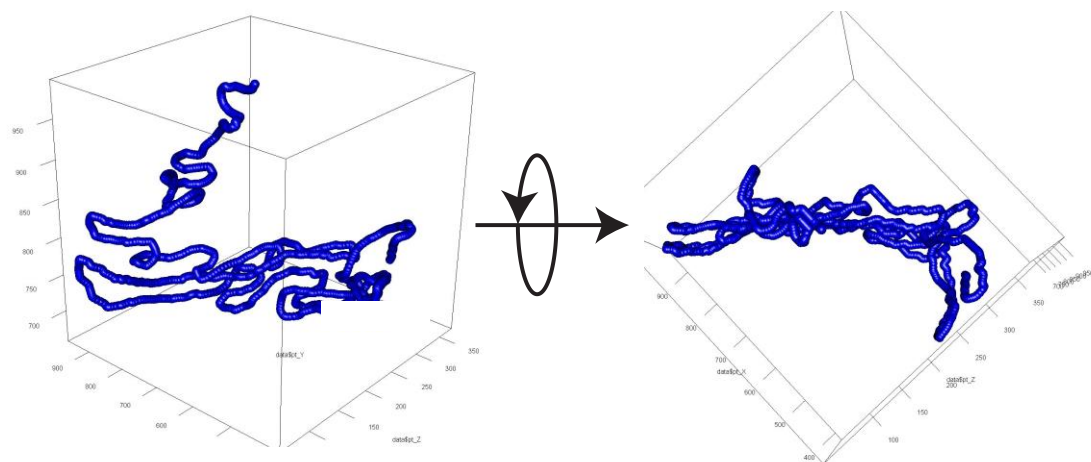
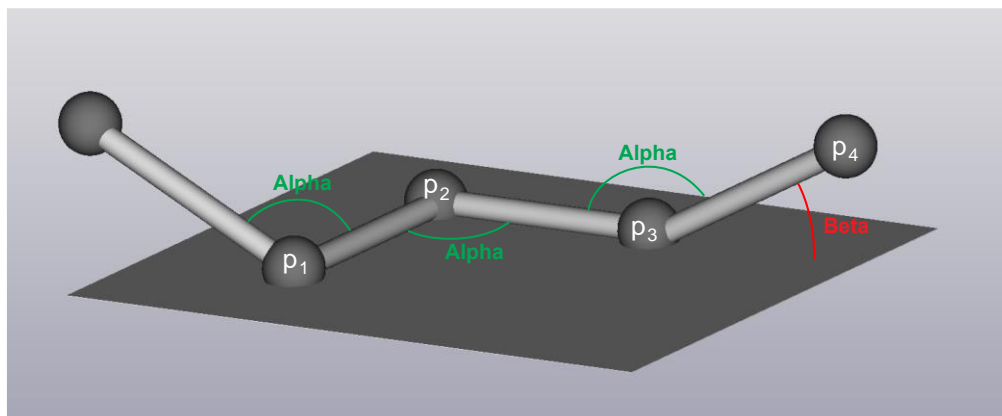
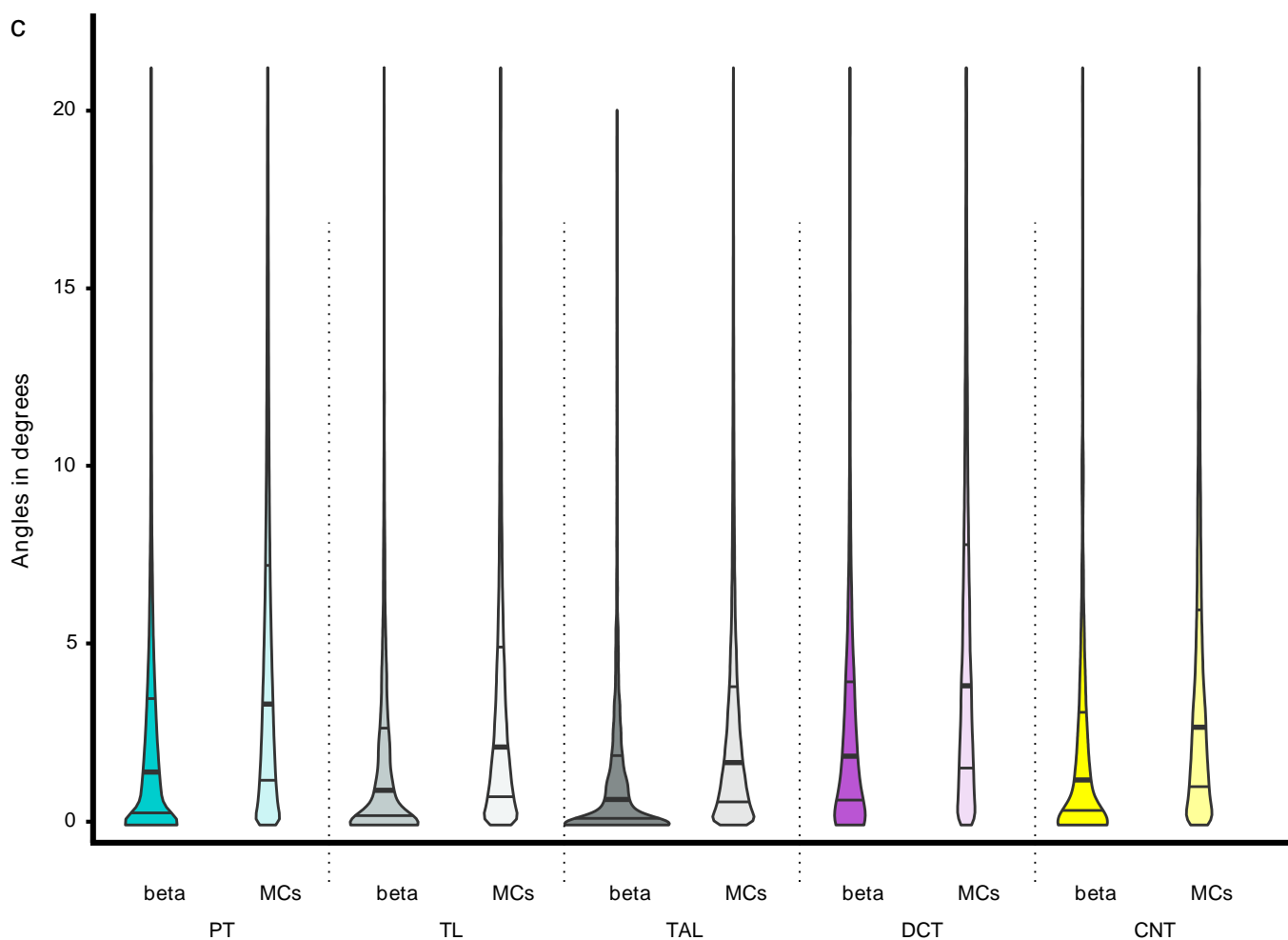


Figure 4

a**b****c****Figure 5**

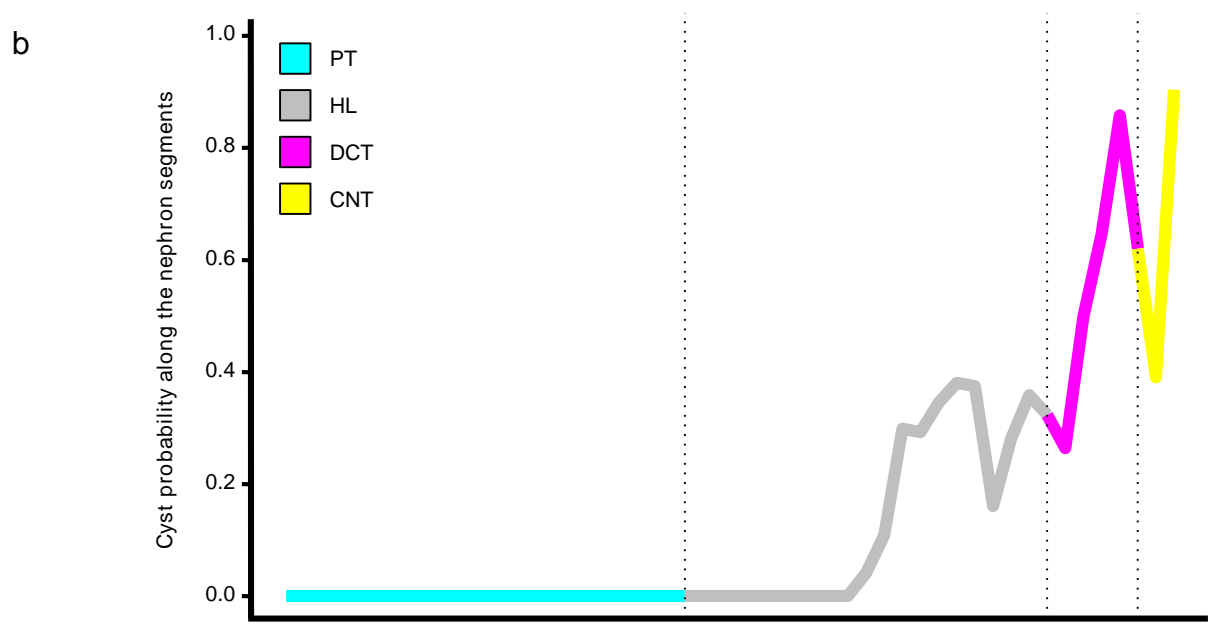
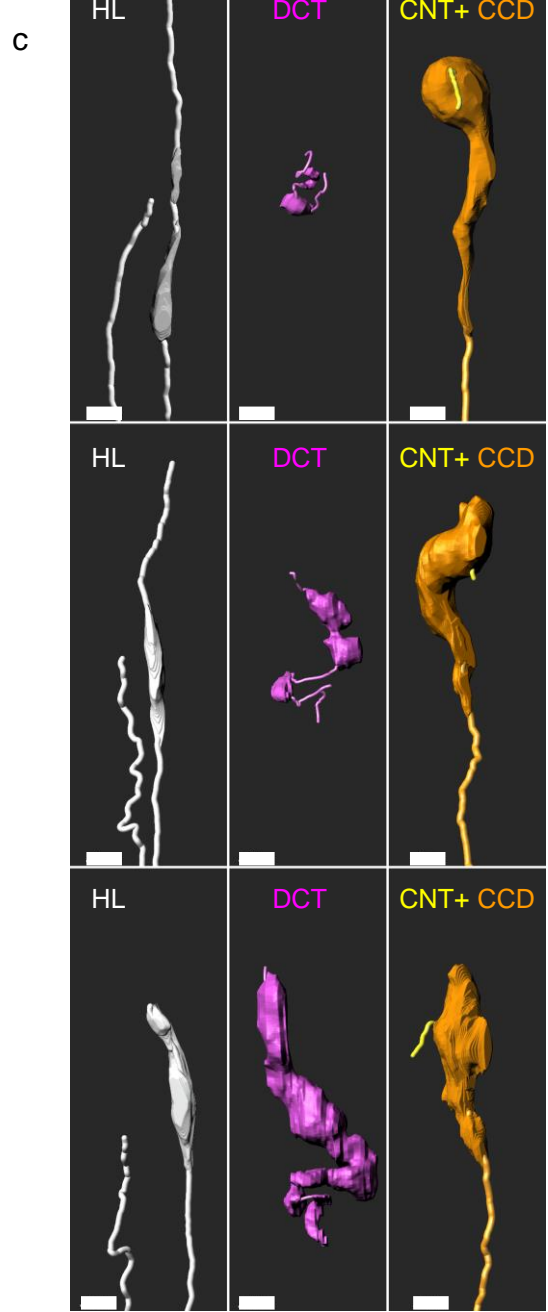
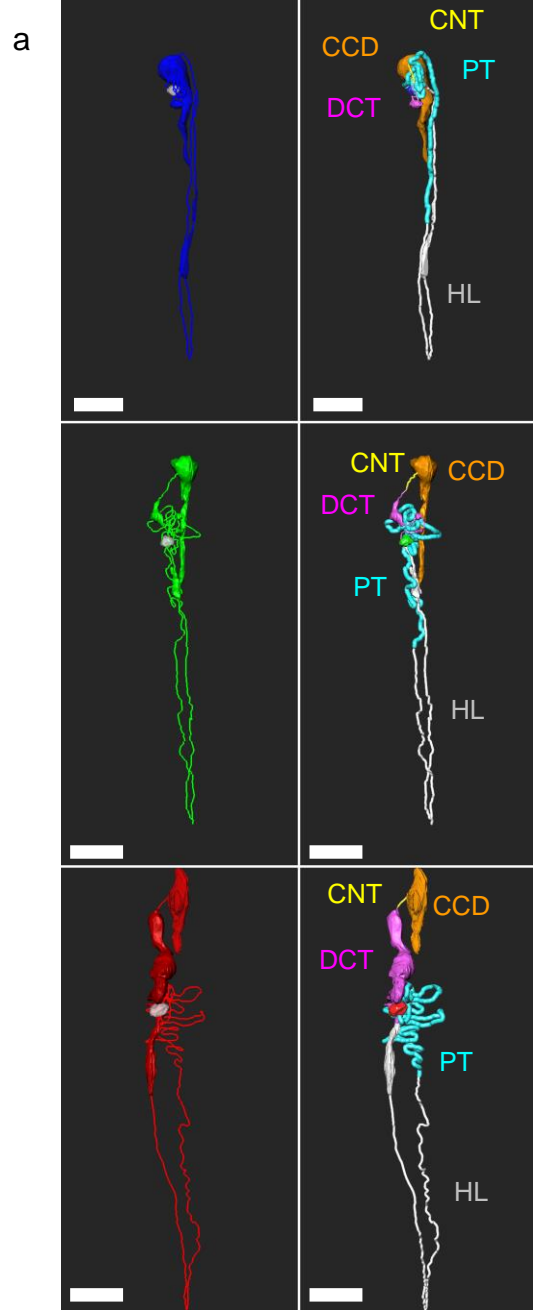


Figure 6

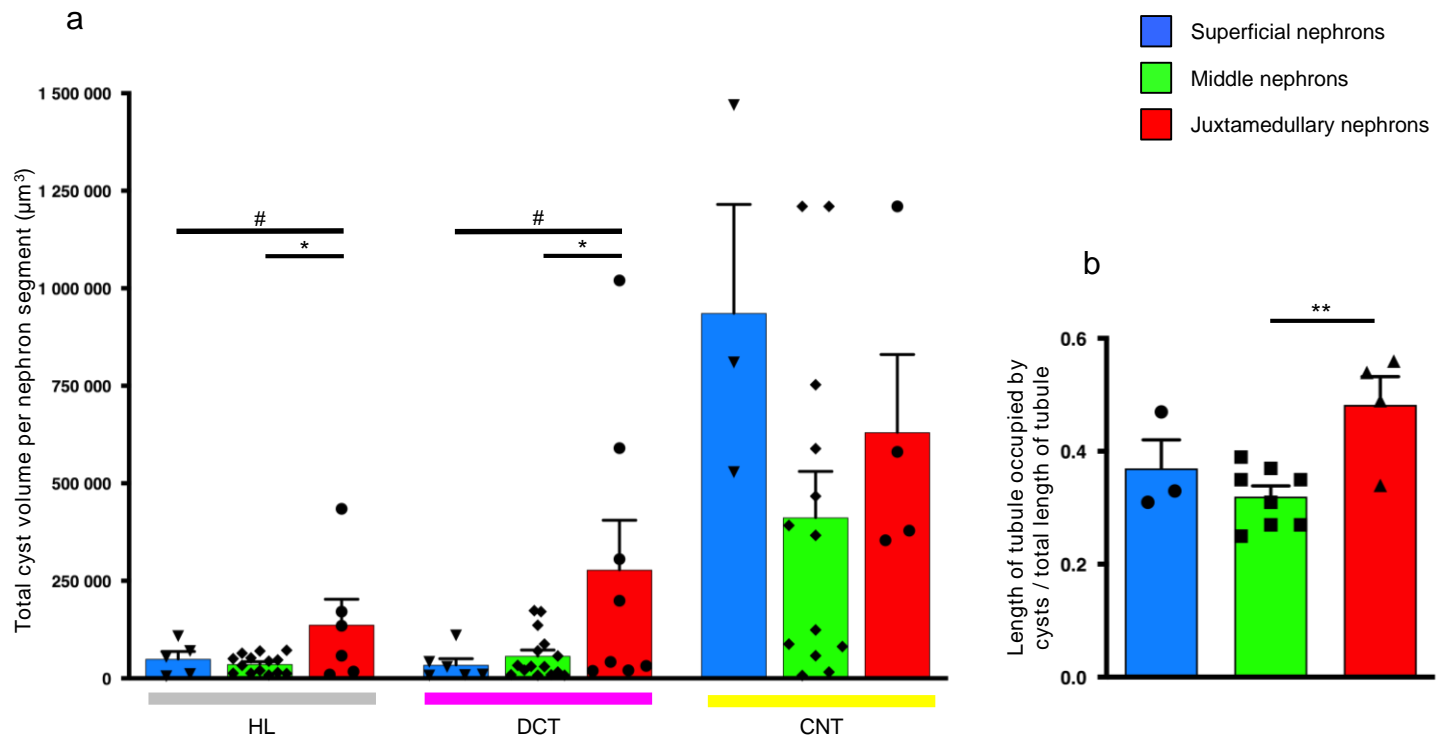
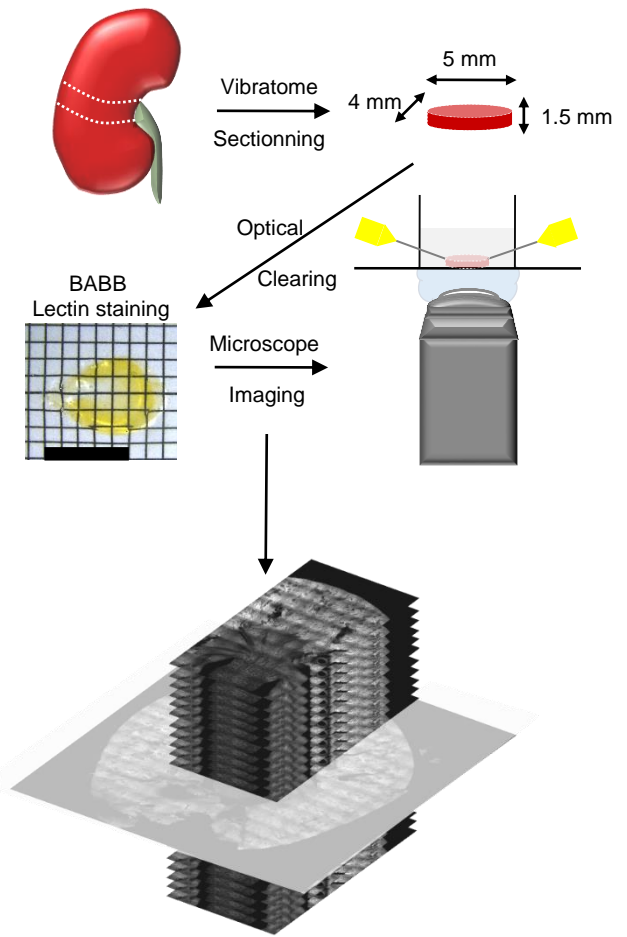


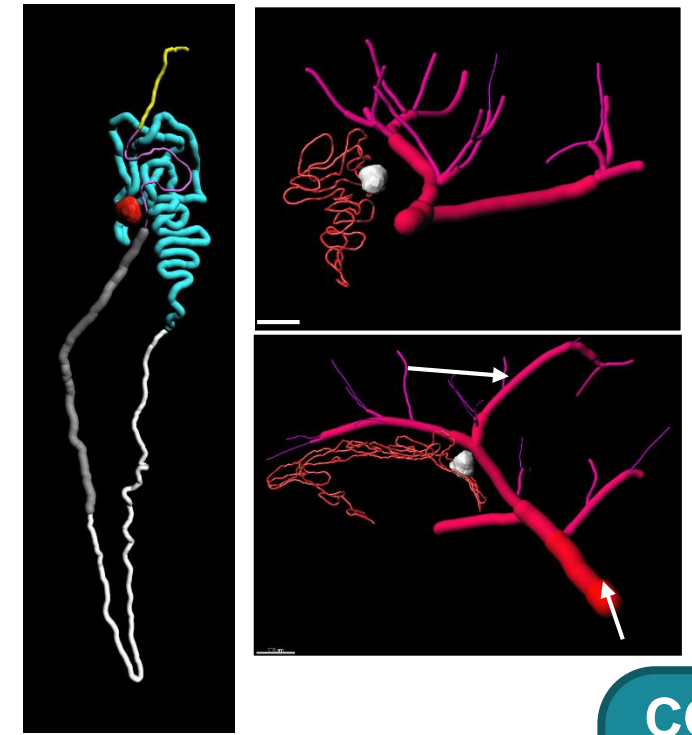
Figure 7

Three-dimensional architecture of nephrons in the normal and cystic kidney.

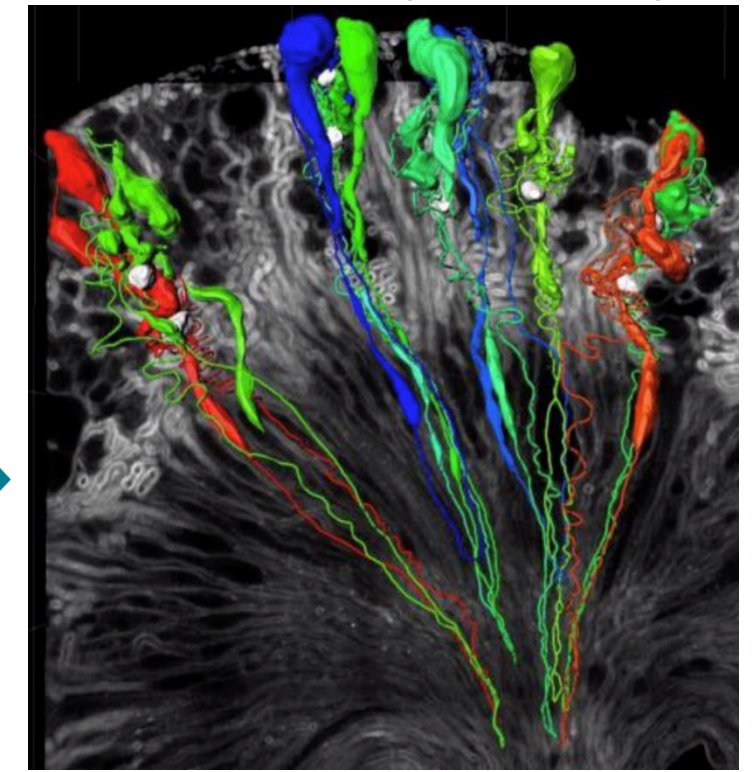
A powerful method



3D Nephrons and vessels reconstruction



3D view of a cystic kidney



CONCLUSION:
A valuable strategy for visualizing the complex structure of kidneys at nephron level in physiological and pathological conditions.